Catal Lett (2012) 142:946–958
DOI 10.1007/s10562-012-0847-8

Low Temperature Ceria-Based Lean NO_x Traps

Jin-Yong Luo · William S. Epling · Gongshin Qi · Wei Li

Received: 27 February 2012 / Accepted: 18 May 2012 / Published online: 6 June 2012

Abstract Using temperature-programmed desorption after NO adsorption at 200 °C, a variety of catalytic materials as potential low-temperature lean NO_x traps were tested after hydrothermal aging. For the non Pt/ceria related materials tested, there was a strong relationship between NO oxidation activity and NO_x storage capacity, regardless of the type of storage phase. While for Pt/ceria containing samples, they exhibited relatively high NO_x trapping ability although they showed relatively poor NO oxidation activity. DRIFTS results indicated that NO_x can be stored via a "nitrite" route for Pt/ceria materials and via a "NO_2" route for the other materials. Among all the materials tested, a Pt/CeO_2/Al_2O_3 sample was found to have the best activity in terms of NO_x trapping and NO oxidation, as compared with samples like Pt/Al_2O_3 and Pt/CeO_2, as well as a commercial LNT. Characterization data showed that the addition of CeO_2 to Pt/Al_2O_3 helped maintain metallic Pt dispersion on Al_2O_3 after aging. Pt sintering on Pt/Al_2O_3 and Pt oxidation on Pt/CeO_2, induced by strong interaction with the support, limited NO oxidation and trapping in the corresponding samples. Besides the stabilization effect on Pt, the addition of CeO_2 introduced more NO_x adsorption sites, which contribute to the enhanced NO_x trapping observed. In addition, Pt dispersion was found to affect stored nitrate stability. Due to enhanced Pt dispersion by ceria modification, nitrates on Al_2O_3 decomposed at much lower temperature on Pt/CeO_2/Al_2O_3 compared to Pt/Al_2O_3.

J.-Y. Luo · W. S. Epling (✉)
Department of Chemical Engineering, University of Waterloo, Waterloo, ON, Canada
e-mail: wsepling@central.uh.edu

G. Qi · W. Li
General Motors Global R&D, Warren, MI, USA

Keywords Lean NO_x trap · CeO_2 · NO oxidation · Thermal aging

1 Introduction

Lean-burn gasoline and diesel engines are typically more fuel efficient than their standard gasoline counterpart, however, NO_x emissions are a significant issue since the traditional three-way catalyst is ineffective for NO_x reduction in a net oxidizing environment. In order to meet current and expected increasingly stringent emission standards, two techniques have been developed and commercialized for NO_x reduction from lean-burn engines, NO_x storage/reduction (NSR), also called the lean NO_x trap (LNT), and NO_x selective catalytic reduction (SCR) [1–6]. For LNTs, the model catalyst typically studied is Pt/BaO/Al_2O_3, which can effectively remove NO_x in the 250–400 °C temperature range, performing relatively poorly at lower temperature due to both limited trapping and regeneration efficiencies [4]. NO_x emissions during engine cold start make up a significant portion of total NO_x emissions during test cycles, with the catalyst remaining below 200 °C for a significant amount of time [5]. Therefore, in order to improve overall emissions performance, one feasible approach is to incorporate components with good low-temperature NO_x trapping ability into the conventional catalyst.

Literature evidence points to four types of materials that show potential as low temperature LNTs, including Al_2O_3-based materials [7–9], $MgAlO_x$ oxides derived from a hydrotalcite precursor [10–16], MnO_x-containing mixed oxides [9, 17, 18] and CeO_2-based composites [19–22]. Xu et al. [7] found that using high-surface-area Al_2O_3 as a NO_x trap material had significant advantages over a conventional barium-based trap at low temperature, in terms of

NO_x conversion and de-sulfurization, due to the lower basicity of Al_2O_3. Kikuyama reported that $Pt/ZrO_2/Al_2O_3$ shows better NO_x sorption ability at low temperature, 200 °C, as compared to Pt/Al_2O_3 and Pt/ZrO_2, and Pt plays an important role in oxidizing NO to NO_2 and subsequently to nitrates ions, which is crucial for NO_x storage at low temperature [8, 9]. Fornasari and coworkers studied novel hydrotalcite-derived low temperature LNTs, such as $Pt/MgAlO_x$ and Pt–Cu/$MgAlO_x$, for light-duty diesel exhaust applications. As compared to conventional $Pt/BaO/Al_2O_3$, these catalysts possess greater low-temperature NO_x storage capacity. Also, these catalysts showed better NO oxidation to NO_2 performance, improved resistance to SO_2 deactivation and lower thermal stability of the stored NO_x, due again to the lower basicity of the $MgAlO_x$ relative to BaO [10–12]. Similar $MgAlO_x$ systems have also been evaluated, i.e. $Co/MgAlO_x$ [13], $Mn/MgAlO_x$ [14], $Pd/MgAlO_x$ [15] and $Ru/MgAlO_x$ [16]. Mn-based mixed oxides, including MnO_x–ZrO_2, MnO_x–CeO_2 and Pd–MnO_x–CeO_2, also show good activity for NO_x storage [17, 18]. The strong oxidation ability of MnO_x and the strong interaction between MnO_x and CeO_2/ZeO_2 contribute to NO_x adsorption on CeO_2 or ZrO_2 in the mixed oxides. CeO_2 or $Ce_xZr_{1-x}O_2$, after Pt addition, also shows good NO_x storage capacity at low temperature [19–22]. In practice, Pt and Ba are supported on ceria-based materials instead of, or with, Al_2O_3 in some commercial LNTs, due to the stabilization of Pt, and also the low temperature NO_x trapping ability of ceria-based materials [23].

Although several types of materials have been proposed as low temperature LNTs, a direct comparison of these, especially after thermal aging, is lacking. Performance after hydrothermal aging is crucial for application since in real operation, the catalyst can be exposed to high temperature, such as during desulfation or particulate filter regeneration. Therefore, in this paper, a variety of materials, as potential LNTs at low temperature, were prepared, and NO_x storage capacity tested after hydrothermal aging. Among them, the best candidate was chosen for further investigation via comparison with its counterparts, in terms of NO oxidation activity, and adsorption and desorption properties. The intrinsic reasons for the improved low temperature NO_x trapping were investigated by structural characterization and structure-performance analysis.

2 Experiment Methodology

2.1 Catalyst Preparation

Al_2O_3 (MI386), promoted by 5 % La, was supplied by Rhodia. BaO/Al_2O_3 (20 %, weight ratio) and CeO_2/Al_2O_3 (20 %) were prepared by a wet impregnation method, using $Ba(OAc)_2$ (Alfa Aesar) and $Ce(NO_3)_3{\cdot}6H_2O$ (Alfa Aesar) precursors. CeO_2 (5 % La promoted) and $CeZrO_x$ (GMR6, 62.1 % CeO_2, 26.5 % ZrO_2) were supplied by AMR and Rhodia, respectively. $MgAlO_x$ was prepared by calcination of a commercial hydrotalcite, HT20 (Sasol), at 500 °C for 4h.

Table 1 Pt loading measured by ICP and BET surface areas

Sample	Fresh Pt/Al_2O_3	Aged Pt/Al_2O_3	Aged $Pt/CeO_2/Al_2O_3$	Aged Pt/CeO_2	Aged $PtPd/Al_2O_3$
% Pt (ICP)	1.0	1.0	1.1	1.1	1.0 (0.2)
S_{BET} (m^2/g)	204	171	128	57	n/m

Pd weight loading percentage is given in parenthesis

n/m not measured

1 wt% Pt was loaded via wet impregnation using a H_2PtCl_6 solution. The catalysts were calcined at 500 °C for 4h. For comparison, a $PtPd/Al_2O_3$ sample was also prepared, by impregnation of Pt/Al_2O_3 with a $Pd(NO_3)_2$ solution, with a nominal Pt:Pd weight ratio of 7:1, which was reported to have the best NO oxidation ability after the same aging conditions [24]. The actual noble metal content measured by inductively coupled plasma (ICP, results shown in Table 1), is close to the nominal loading.

$MnZrO_x$ (Mn:Zr = 3:7) and $MnCeZrO_x$ (Mn:(Ce + Zr) = 3:7, Ce/Zr = 2:1) were prepared using a co-precipitation method. Metal precursors (total 0.2 mol) $Mn(NO_3)_2$ (50 wt% solution), $Ce(NO_3)_3{\cdot}6H_2O$ and $ZrO(NO_3)_2$, were dissolved into 500 mL H_2O at room temperature. An NH_3 solution (28 %) was added dropwise while stirring until the pH reached 9. At pH 9, stirring was maintained for 1 h, then the suspension was held for another 1 h without stirring. After filtration and washing, the obtained precipitate was dried at 120 °C and calcined at 500 °C for 4 h.

The obtained powder catalysts (10 g) were mixed with H_2O (25 g) and a small amount of Al_2O_3 sol binder (Aremco, 1 g), and ball milled at room temperature overnight. The powder catalysts were then washcoated on a blank cordierite monolith (0.75′ (D) × 1′ (L), 400 CPSI), with a loading of 200 g/L (57 g/ft^3 Pt). Finally, the obtained monolithic catalysts were hydrothermally aged at 750 °C for 72 h in air with 10 % H_2O content. For comparison purposes, a commercial sample supplied by Umicore was also tested, with a washcoat loading of 300 g/L (contains Ba, oxygen storage materials, 100 g/ft^3 Pt, 40 g/ft^3 Pd and 5 g/ft^3 Rh).

2.2 Performance Check

The monolithic samples (0.75′ (D) × 1′ (L)) were tested in a quartz tube reactor, mounted in a Lindberg furnace. The

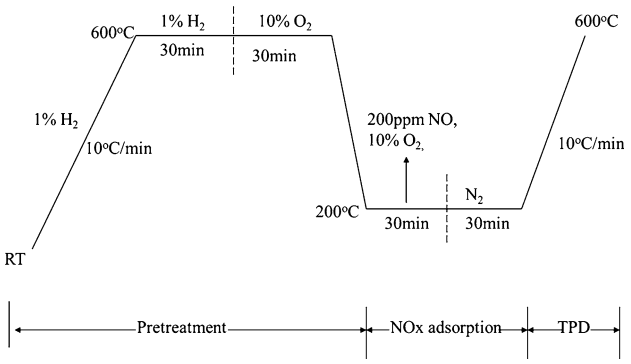

Fig. 1 Reaction protocol for catalyst performance evaluation

sample temperature was measured by a K-type thermocouple placed just inside a channel at the catalyst upstream face. Lean and rich gas mixtures were prepared separately using mass flow controllers (Brooks) and introduced to the reactor by a switching valve. Outlet gases were analyzed with a calibrated fourier transform infrared (FTIR) analyzer (ThermoNicolet NEXUS 670). The performance was checked by temperature programmed desorption of NO_x (NO_x-TPD), with the protocol shown in Fig. 1. First, the sample was pretreated at 600 °C in 1 % H_2/N_2 for 30 min, then in 10 % O_2/N_2 for another 30 min. The sample was then cooled to 200 °C and 200 ppm NO and 10 % O_2 were introduced for 30 min. After NO_x and O_2 were removed, the sample was exposed to N_2 for 30 min to allow weakly adsorbed species to desorb. Finally, a TPD run was performed in N_2 from 200 to 600 °C, with a heating rate of 10 °C/min. The gas hourly space velocity (GHSV) was kept at 25,000 h^{-1}, and 8 % CO_2 and 5 % H_2O were always present, i.e. were present in each stage of the test. By replacing NO with NO_2, NO_x-TPD experiments with NO_2 adsorption were also performed.

NO oxidation was tested on the catalysts after the same pretreatment. A gas mixture containing 200 ppm NO, 10 % O_2, 8 % CO_2 and 5 % H_2O, balanced by N_2 was used, at a GHSV of 25,000 h^{-1}. The reaction was evaluated from 150 to 550 °C, with 50 °C increments. At each temperature, the conditions were held for 30 min in order to achieve steady-state conditions, which were met based on the outlet NO_x concentration equaling that of the inlet.

2.3 Characterization

Specific surface areas were measured by N_2 adsorption at liquid nitrogen temperature using a Micromeritics 2010 apparatus, with values listed in Table 1. ICP data were collected on a Varian radial torch Vista Pro, and measured Pt loadings are listed in Table 1. About 100 mg of the sample was dissolved using mineral acids. Once dissolution was complete, the sample was diluted to 100 mL and analyzed by ICP. X-ray diffraction (XRD) patterns were recorded on a Rigaku D/MAX-RB diffractometer with Cu Kα radiation ($\lambda = 1.5418$ Å) operated at 40 kV and 100 mA. X-ray photoelectron spectroscopy (XPS) was performed on a Physical Electronics Quantera. Data were collected at a 112 eV pass energy for Pt, using adventitious carbon to charge shift based on C 1s = 284.8 eV.

Transmission electron microscope (TEM) images were collected on a JEOL JEM-2100F scanning/TEM (S/TEM) with a probe aberration corrector equipped with an Oxford energy dispersive X-ray spectrometer (EDS). The S/TEM was operated at an acceleration voltage of 200 kV. The S/TEM specimens were prepared by ultrasonically dispersing a small portion of the sample in methanol and placing a drop of the dispersion on a lacy carbon TEM grid.

CO adsorption was characterized using diffuse reflectance infrared fourier transform spectroscopy (DRIFTS) in order to investigate the dispersion state of Pt, and DRIFTS of NO adsorption was performed to characterize NO_x adsorption sites and mechanisms. Both experiments were performed on a ThermoNicolet NEXUS 670. Gases were mixed by mass flow controllers and introduced into the DRIFTS reactor at a rate of 100 mL/min. For CO adsorption, the sample was pre-treated at 600 °C in 1 % H_2/He for 30 min. Then after decreasing to RT and obtaining the background spectrum, it was exposed to 1 % CO/He for 5 min. The spectrum was obtained after exposing the sample to He for another 5 min, until the gas phase CO band disappeared. For NO adsorption, the sample was pretreated at 600 °C in 1 % H_2/He for 30 min, then in 10 % O_2/He for another 30 min. After cooling to 200 °C, a background was obtained. Then, 200 ppm NO and 10 % O_2 balanced by He was introduced, and spectra at different times were recorded. In order to explore the thermal stability of the stored NO_x, spectra were also obtained during TPD.

3 Results and Discussion

3.1 NO_x Storage Capacity by TPD

Table 2 summarizes the results of the NO_x adsorption and TPD experiments and includes the total amount of NO_x adsorbed, NO oxidation to NO_2 conversions (obtained at the end of the adsorption period where steady-state NO_2 concentrations were observed), peak NO_x desorption temperatures during the TPD and desorbed NO_2 percentages. The desorption profiles of four of the samples, Pt/Al_2O_3, Pt/CeO_2, $Pt/CeO_2/Al_2O_3$ and $PtPd/Al_2O_3$, are shown in Fig. 2. From Table 2, the NO_x (NO as the "source") adsorbed at 200 °C decreased in the following sequence: $Pt/CeO_2/Al_2O_3$ > commercial ≈ $PtPd/Al_2O_3$ > Pt/CeO_2 > Pt/Al_2O_3 ≈ $Pt/CeZrO_2$ > $Pt/BaO/Al_2O_3$ > $Pt/MgAlO_x$

Table 2 Summary of NO_x storage amounts, surface NO_x species decomposition temperatures and NO oxidation activity during NO_x-TPD for all the samples tested, with NO as the feed NO_x source

Sample	NO_x storage at 200 °C (μmol/g washcoat)	T of NO peak (°C)	T of NO_2 peak (°C) and NO_2 (%)	NO oxidation to NO_2 (%) at 200 °C
$Pt/BaO/Al_2O_3$	18	483	n/a	17.5
Pt/Al_2O_3	21 (151)	485 (463)	n/a (390)	18.4
$Pt/CeO_2/Al_2O_3$	41 (126)	390	360, 68 % (345)	24
Pt/CeO_2	27 (124)	282, 390	375, 62 % (310)	1.9
$Pt/CeZrO_x$	20	292	381, 57 %	5
$Pt/MgAlO_x$	10	393	410, 41 %	11
$MnZrO_x$	6	250	n/a	13
$MnCeZrO_x$	10	250	250, 30 %	11.5
CeO_2	0 (124)	n/a	n/a (370)	0
$PtPd/Al_2O_3$	34	424	400, 24 %	24
Commercial[a]	35	435	435, 8 %	5

NO_x storage amounts tested using NO_2 as NO_x source are given in parentheses

[a] Commercial: washcoat 300 g/L, 100 g/ft^3 Pt, 40 g/ft^3 Pd and 5 g/ft^3 Rh (also Ba, OSC)

n/a none

$\approx MnCeZrO_x > MnZrO_x > CeO_2$. The $Pt/CeO_2/Al_2O_3$ adsorbed the most, 41 μmol/g, which was higher than the adsorbed amount on the commercial sample with a higher noble metal loading, and much higher than the amount adsorbed on the conventional $Pt/BaO/Al_2O_3$ catalyst.

With respect to the desorption behaviour of both Pt/Al_2O_3 and $Pt/BaO/Al_2O_3$, as shown in Fig. 2, NO_x desorbed as NO at high temperature, with the peak at 485 °C. The addition of Pd to Pt/Al_2O_3 decreased the desorption temperature by 60 °C. In contrast, most of the NO_x was desorbed as NO_2 from the ceria-containing samples, i.e. Pt/CeO_2, $Pt/CeZrO_2$ and $Pt/CeO_2/Al_2O_3$, with the peak desorption temperatures below 400 °C. Among these, the NO_x desorption behaviour of $Pt/CeO_2/Al_2O_3$ and Pt/CeO_2 was quite similar.

$Pt/CeO_2/Al_2O_3$ had the highest NO_x storage capacity and the highest NO oxidation activity, with a 24 % NO to NO_2 conversion at 200 °C. On the other hand, pure CeO_2 showed almost no NO oxidation conversion at 200 °C and did not store NO at this temperature. Based on these results, there seems to be a relationship between NO oxidation and NO_x storage. Therefore, in Fig. 3, NO_x storage capacities were plotted as a function of NO oxidation (using the data listed in Table 2). If the Pt/oxygen-storage-component (OSC, where here OSC refers to the ceria-containing samples) containing samples are excluded, a good relationship between NSC (NO_x storage capacity) and NO oxidation is obtained, regardless of the sample type and storage phase; namely, the higher the NO oxidation conversion, the higher the NO_x storage amount, indicating the importance of NO oxidation to NO_x storage. This is consistent with the general proposal that NO oxidation to NO_2 is the first crucial step for NO_x storage (1). However, very interestingly, for Pt supported on ceria-based samples, relatively high NO_x storage capacities were obtained although they exhibited relatively low NO oxidation ability, which suggests that NO was stored via another route, instead of a route requiring NO_2, over the Pt/OSC-containing samples.

Although NO oxidation was relatively poor, such that NO is possibly not stored via a NO_2 precursor route, this does not preclude NO_2 storage being inefficient over Pt/OSC materials. Therefore, NO_x storage using NO_2 as the NO_x source was also evaluated with some of the samples, including Pt/Al_2O_3, $Pt/CeO_2/Al_2O_3$, Pt/CeO_2 and pure CeO_2, and the results of both adsorption and the TPD are shown in Fig. 4. During adsorption, once NO_2 was introduced, NO was observed in the effluent. With extended time, the NO concentration decreased, as well as the overall NO_x adsorption rate. From this, we can deduce that NO_2 was mainly adsorbed via disproportionation [25], with the equation being:

$$3NO_2 + O^{2-} \rightarrow 2NO_3^- + NO \quad (1)$$

The initial NO_x uptake rate decreased in the following order: $Pt/CeO_2 > Pt/CeO_2/Al_2O_3 > Pt/Al_2O_3 > CeO_2$. From the TPD profiles, the total amounts of NO_x adsorbed using NO_2 as the NO_x source were calculated, and the results are shown in Table 2 (in parentheses). As compared with those using NO as the NO_x source, much higher NO_x storage amounts were observed using NO_2. Among them, Pt/Al_2O_3 adsorbed the largest amount of NO_x, around 150 μmol/g, and Pt/CeO_2, CeO_2 and $Pt/CeO_2/Al_2O_3$ adsorbed similar amounts, which obviously differs from the trends observed with NO adsorption. If calculated based on surface area (surface areas listed in Table 1), $Pt/CeO_2 > Pt/CeO_2/Al_2O_3 > Pt/Al_2O_3$, and Pt/CeO_2 adsorbs more than double the amount of NO_x when compared with Pt/Al_2O_3. With NO_2 as the NO_x source in the feed gas, the NO oxidation limitation is excluded, and the data suggest that CeO_2 actually has a higher intrinsic capacity for NO_x adsorption than Al_2O_3 based on surface area. Also interestingly, although the addition of Pt to CeO_2 did enhance the initial NO_x adsorption rate, it did not change the total amount of adsorbed NO_x.

With respect to the desorption process, most of the NO_x was desorbed as NO_2 from the ceria-containing samples, with the peak desorption temperatures less than 400 °C,

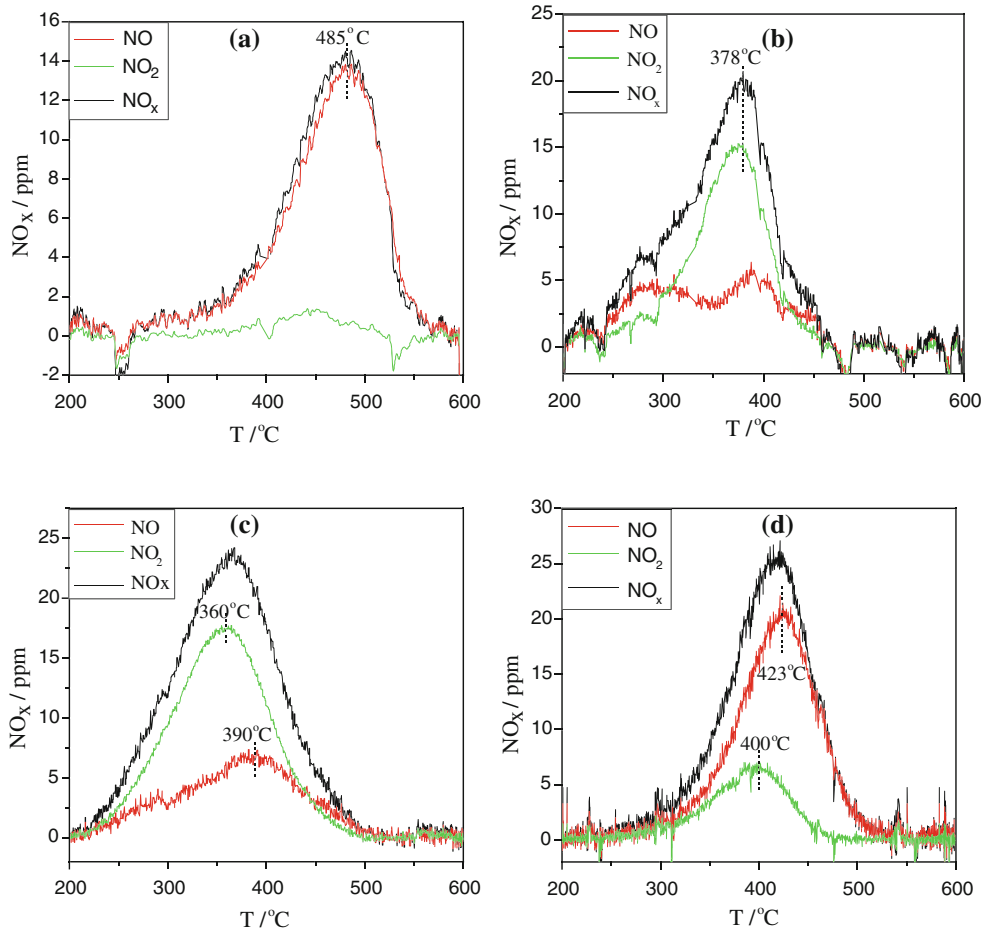

Fig. 2 NO_x concentration profiles [NO_x (*black*), NO_2 (*green*) and NO (*red*)] during temperature programmed desorption for **a** Pt/Al_2O_3, **b** Pt/CeO_2, **c** $Pt/CeO_2/Al_2O_3$ and **d** $PtPd/Al_2O_3$ (NO_x adsorption: 200 ppm NO, 10 % O_2, 8 % CO_2, 5 % H_2O, balance N_2, SV = 25,000 h^{-1}, 200 °C; desorption: 8 % CO_2, 5 % H_2O, balance N_2, SV = 25,000 h^{-1}, 200–600 °C, 10 °C/min)

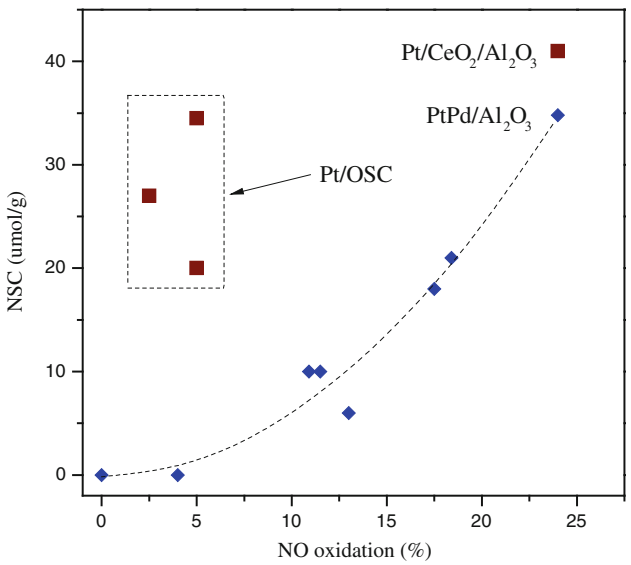

Fig. 3 Relationship between NO_x storage capacity and NO oxidation to NO_2

consistent with those observed during the TPD after NO adsorption. Comparing CeO_2 and Pt/CeO_2, Pt promotes NO_x decomposition, with the desorption temperature lowered by 60 °C. For Pt/Al_2O_3, besides a similar high-temperature NO desorption peak, a lower temperature NO_2 desorption peak is also observed at 390 °C, possibly due to NO_x desorbing from relatively weaker adsorption sites as NO_x coverage becomes higher.

In summary, Pt/OSC samples adsorb NO through a non-NO_2 route, while the other samples tested adsorb NO_x via a NO_2 route, leading to a strong relationship between NSC and NO oxidation. Using NO_2 as the NO_x source is far more efficient for NO_x storage than using NO. The addition of Pt to CeO_2 does not enhance the NO_2 adsorption capacity, but promotes NO_x uptake and NO_x release. This again demonstrates that for application, NO oxidation to NO_2 is beneficial for NO_x storage. And with typical engine exhausts containing NO_x mainly as NO (~90 %) instead of NO_2, this points to the need for upstream oxidation catalysts.

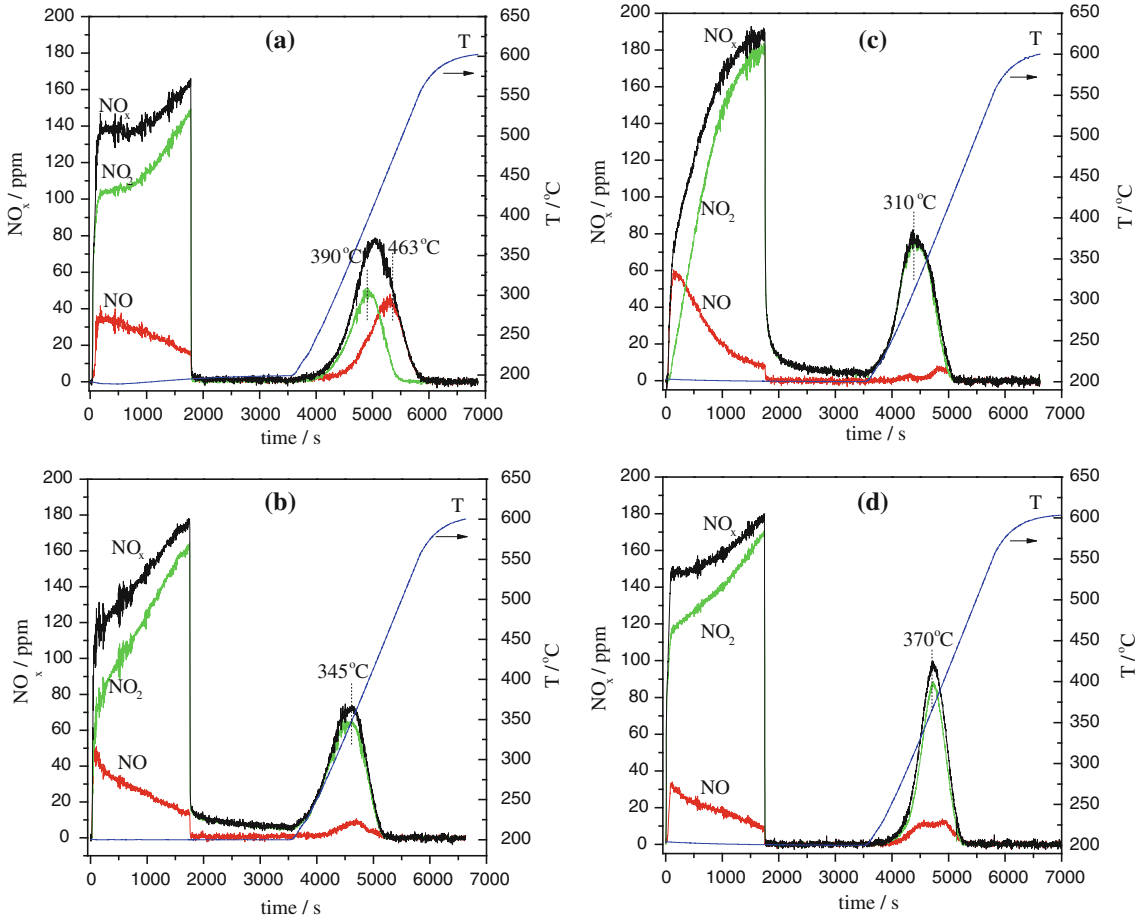

Fig. 4 NO_x concentration profiles during NO_2 adsorption and temperature programmed desorption for **a** Pt/Al_2O_3, **b** $Pt/CeO_2/Al_2O_3$, **c** Pt/CeO_2 and **d** CeO_2 (reaction conditions similar to Fig. 2 but using 200 ppm NO_2 instead of NO)

3.2 NO Oxidation to NO_2

As mentioned above, NO oxidation significantly benefits the NO_x storage process, especially at low temperature. Therefore, NO oxidation was investigated over Pt/Al_2O_3, Pt/CeO_2, $Pt/CeO_2/Al_2O_3$ and a reference $PtPd/Al_2O_3$ catalyst, and the results are shown in Fig. 5. Among these, $Pt/CeO_2/Al_2O_3$ and $PtPd/Al_2O_3$ were the most active. In this study, all catalysts were hydrothermally aged at 750 °C for 72 h, and it is worth noting that the addition of a small amount of Pd to Pt/Al_2O_3 significantly promoted its activity, with the well-known reason being stabilization of Pt against sintering by Pd [24]. Therefore, it seems that Pt/Al_2O_3 had an insufficient number of active sites, due to Pt sintering after aging (details discussed below), which limits the reaction, and even at very high temperature, thermodynamic equilibrium conversion is not achieved. On the other hand, although ceria is reported to stabilize Pt [26–28], Pt/CeO_2 is relatively inactive towards NO oxidation, especially at low temperature.

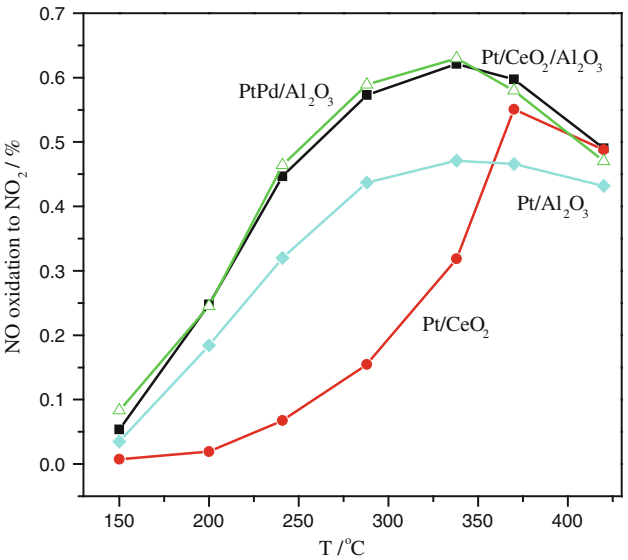

Fig. 5 NO oxidation to NO_2 Pt/Al_2O_3 (*cyan*), Pt/CeO_2 (*red*), $Pt/CeO_2/Al_2O_3$ (*black*) and $PtPd/Al_2O_3$ (*green*) (200 ppm NO, 10 % O_2, 8 % CO_2, 5 % H_2O, balance N_2, SV = 25,000 h^{-1})

3.3 Adsorption Sites and Mechanism by DRIFTS

The results in Fig. 3 suggest two routes for NO storage in the presence of O_2. In an attempt to determine the storage mechanism(s), as well as what types of storage sites exist, DRIFTS data were obtained during NO adsorption and the results are shown in Fig. 6, with the band assignments summarized in Table 3.

DRIFTS spectra of NO/O_2 adsorption on Pt/Al_2O_3 (La-doped) at 200 °C as a function of adsorption time are shown in Fig. 6a. Typical bands for nitrites and nitrates were evident, such as bridging nitrite (1,230 and 1,315 cm^{-1}), linear nitrite (1,467 cm^{-1}), bridging nitrate (1,615 cm^{-1}), chelating nitrate (1,581 and 1,293 cm^{-1}) and monodentate nitrate (1,557 cm^{-1}). The associated bands for bridging nitrate at ~1,210 cm^{-1} and monodentate nitrate at ~1,257 cm^{-1} are probably overlapped by the strong nitrite band at 1,230 cm^{-1}. Also, a band at 1,197 cm^{-1} is observed, which has not previously been reported on Al_2O_3 or Pt/Al_2O_3. Another Pt/Al_2O_3 sample, with no La, was characterized and this peak was not evident. Thus, the 1,197 cm^{-1} peak must be related to La-related NO_x species. Literature evidence has shown that NO adsorbed on a 40 % La_2O_3/Al_2O_3 sample or bulk La_2O_3, as NO^-, results in a band at 1,195 cm^{-1} in DRIFTS [32], further verifying this assignment. This band changes similarly to bridging nitrite over Al_2O_3. With exposure time, all the bands gradually increased, especially in the first 15 min.

The DRIFTS spectra shown in Fig. 6b were obtained during NO_x adsorption on $Pt/CeO_2/Al_2O_3$ and are quite similar to those obtained from Pt/Al_2O_3. The same nitrite and nitrate bands developed with extended NO_x exposure time. The only difference is the appearance of a small band

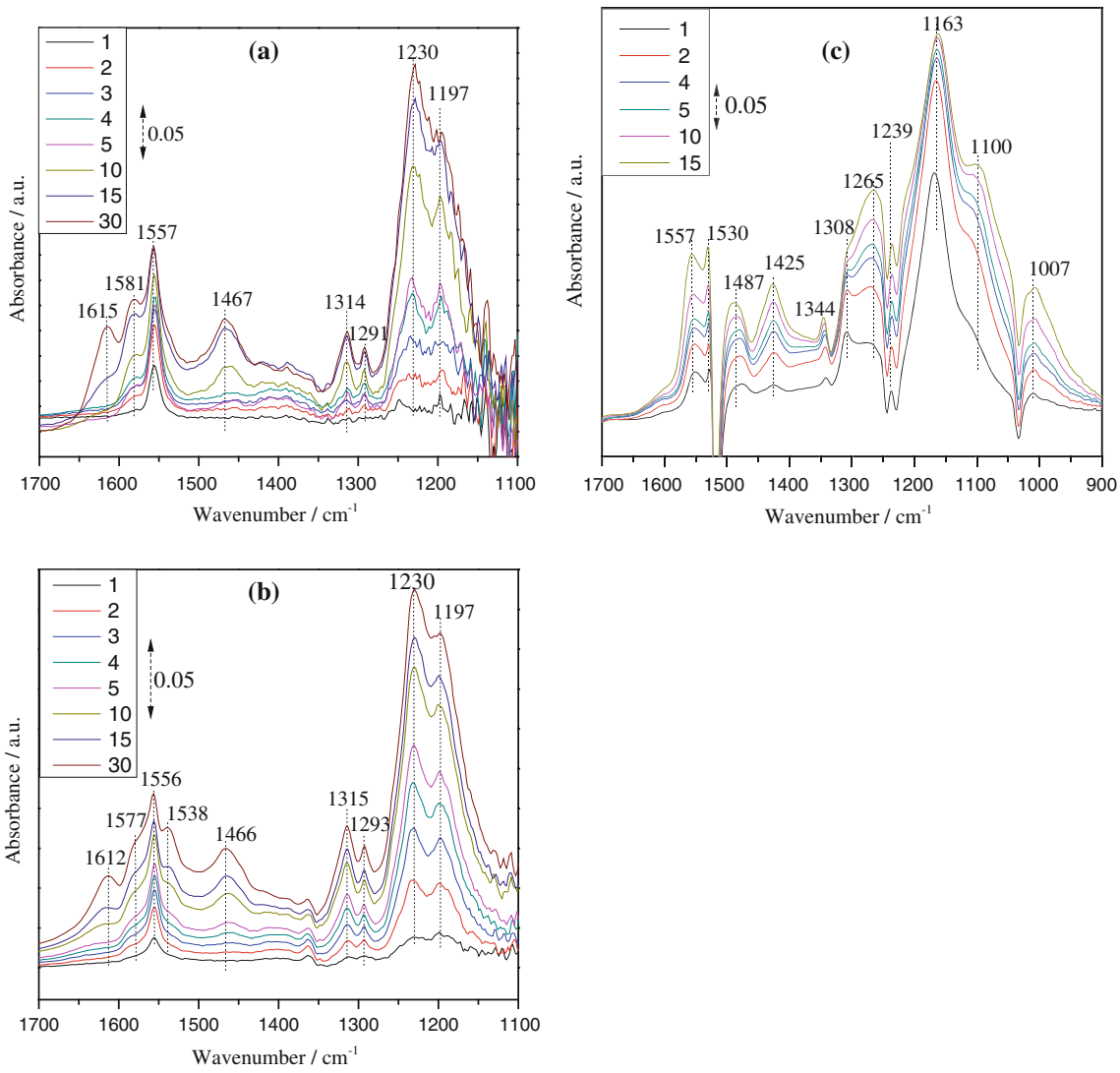

Fig. 6 DRIFTS spectra during NO/O_2 adsorption at different time (min) over **a** Pt/Al_2O_3, **b** $Pt/CeO_2/Al_2O_3$ and **c** Pt/CeO_2

Table 3 DRIFTS assignments of adsorbed NO_x species [22, 29–34]

Surface species	Frequencies (cm^{-1})	Assignments
Linear nitrites on Al_2O_3	1,460	V (N=O)
Bridging bidentate nitrites on Al_2O_3	1,302	V_{as} (NO_2)
	1,230[a]	V_s (NO_2)
Bridging bidentate nitrates on Al_2O_3	1,610[a]	V_s (NO_2)
	1,210	V_{as} (NO_2)
Chelating bidentate nitrates on Al_2O_3	1,590[a]	V_s (NO_2)
	1,297	V_{as} (NO_2)
Monodentate nitrates on Al_2O_3	1,550[a]	V_{as} (NO_2)
	1,257	V_s (NO_2)
NO^- on La_2O_3	1,197	V_{as} (NO)
Bidentate nitrites on CeO_2	1,162[a]	V_s (NO_2)
	1,308	V_{as} (NO_2)
Bridging bidentate nitrates on CeO_2	1,595[a]	V_s (NO_2)
	1,215[a]	V_{as} (NO_2)
	1,001	V_s (NO_3)
Chelating bidentate nitrates on CeO_2	1,565[a]	V_s (NO_2)
	1,236[a]	V_a (NO_2)
	1,030–1,000	V_s (NO_3)
Monodentate nitrates on CeO_2	1,530[a]	V_{as} (NO_2)
	1,250–1,275[a]	V_s (NO_2)
	1,027	V_s (NO_3)

[a] Strongest band

at 1,538 cm^{-1}, which can be assigned to monodentate nitrates on ceria. Only monodentate nitrates were observed, while other forms of nitrates, such as chelating or bridging bidentate nitrates, may also form but were overlapped by nitrates bound on alumina. Although both alumina and ceria adsorbed NO_x, it appears that most of the NO_x was still adsorbed on the Al_2O_3 surface, based on band intensities.

The DRIFTS spectra shown in Fig. 6c were obtained during NO_x adsorption on Pt/CeO_2 and are quite different from the previous two sets. Once NO/O_2 was introduced, a band at 1,163 cm^{-1}, assigned to bidentate nitrites on ceria, appeared very quickly and reached near saturation within 4 min. With longer exposure time, nitrate bands slowly developed, such as chelating bidentate nitrates (1,557, 1,265 and 1,007 cm^{-1}) and monodentate nitrates (1,530 cm^{-1}).

The results of DRIFTS for NO/O_2 adsorption over the different catalysts at 200 °C suggest different adsorption mechanisms. For Pt/Al_2O_3 and $Pt/CeO_2/Al_2O_3$, both nitrites and nitrates develop with time simultaneously, while for Pt/CeO_2, nitrites form first, followed by nitrates. Based on the types of adsorbed NO_x species, two reaction pathways have been proposed in the literature regarding NO adsorption on $Pt/Ba/Al_2O_3$ catalysts, including a "nitrate (or NO_2) route" and a "nitrite route" [25]. Combined with the NO oxidation activity, which was relatively high over the Al_2O_3-based catalysts and low on Pt/CeO_2, we can deduce that NO_x is stored via a "NO_2" intermediate route on Pt/Al_2O_3 and $Pt/CeO_2/Al_2O_3$ as nitrites and nitrates, while via a "nitrite" route on Pt/CeO_2.

The NO_x-TPD profile of $Pt/CeO_2/Al_2O_3$ in Fig. 2 is very similar to Pt/CeO_2, in terms of both desorption temperature and product distribution (NO_2 vs. NO), which would suggest that NO_x is mainly stored on ceria, while the DRIFTS results indicate that a large portion of NO_x is adsorbed over Al_2O_3. DRIFTS data were obtained during TPD in an attempt to resolve this apparent discrepancy, and the results are shown in Fig. 7.

The DRIFTS spectra during TPD of NO_x species from Pt/Al_2O_3 are shown in Fig. 7a. With increasing temperature, the nitrite bands decreased in intensity and disappeared by 400 °C. The bidentate nitrate features, both bridging and chelating, also decreased and were not evident by 300 °C. On the other hand, monodentate nitrates grew in intensity, indicating nitrites and some nitrates were being converted into more stable monodentate nitrates. Similarly, DRIFTS spectra obtained from $Pt/CeO_2/Al_2O_3$, shown in Fig. 7b, show a decrease in nitrite band intensities, as well as some nitrate bands, including ceria nitrates, and an increase in monodentate nitrates on Al_2O_3. The differences, as compared to Pt/Al_2O_3, are the lower temperatures for nitrate decomposition. For example, monodentate nitrates on Al_2O_3 for $Pt/CeO_2/Al_2O_3$ start to decompose above 450 °C, while the same nitrates are stable even at 550 °C on Pt/Al_2O_3. DRIFTS spectra obtained from Pt/CeO_2 during TPD are shown in Fig. 7c. Very clearly, nitrite bands decrease and nitrate bands (bridging at 1,595 cm^{-1}, chelating at 1,565 cm^{-1} and monodentate 1,530 cm^{-1}) increase until 400 °C. After that, all nitrates start to decompose.

In Fig. 8, the relative stability of nitrite and nitrates are compared for these three samples, including a fresh Pt/Al_2O_3 sample. Nitrates on Pt/CeO_2 and $Pt/CeO_2/Al_2O_3$ have the same stability until 450 °C, while nitrates on Pt/Al_2O_3 are much more stable, at least up to 550 °C. Such a sequence is consistent with NO_x-TPD results shown in Fig. 2. Overall, desorption temperatures here were slightly higher, which is possibly due to the different reactors, but more likely the absence of H_2O and CO_2.

Again, the DRIFTS results indicate that nitrates are adsorbed on Al_2O_3 for the $Pt/CeO_2/Al_2O_3$ sample, while reactor data (TPD) seemingly shows that NO_x is mainly adsorbed on CeO_2, based on the comparison with Pt/Al_2O_3 and Pt/CeO_2. Although the DRIFTS and reactor data show seemingly contradictory results, when the TPD data of $Pt/CeO_2/Al_2O_3$ is compared to data obtained from a fresh Pt/Al_2O_3 sample, the TPD profiles match. This is due to the dispersion of Pt being maintained with ceria added to the

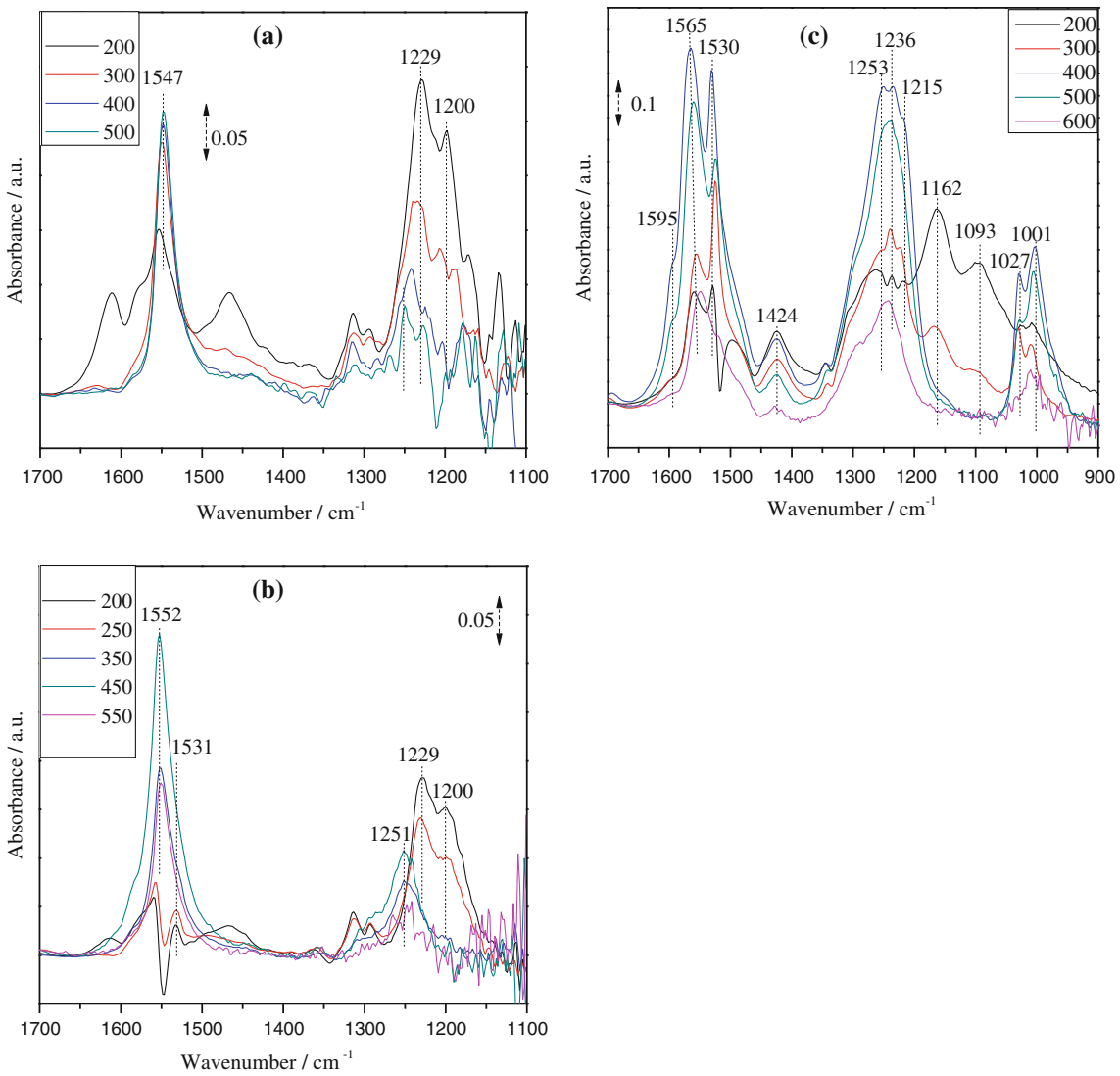

Fig. 7 DRIFTS spectra during desorption at different temperatures over **a** Pt/Al_2O_3, **b** $Pt/CeO_2/Al_2O_3$ and **c** Pt/CeO_2

formulation, as will be clearly shown below in the "Characterization" section. Thus, the two techniques actually are consistent. These data demonstrate that although ceria can adsorb NO_x, due to its relatively small amount and low coverage on the support, the NO_x is indeed mainly stored on the alumina.

3.4 Structural Characterization

To better understand the possible changes the ceria induced, XRD, CO adsorption, XPS and TEM were used to characterize the samples. XRD patterns obtained from Pt/Al_2O_3, Pt/CeO_2 and $Pt/CeO_2/Al_2O_3$ are shown in Fig. 9. Typical reflections of CeO_2 and γ-Al_2O_3 are observed. Sharp and intense reflections at around 40°, 46°, 67.5° and 81.3° are also apparent for the Pt/Al_2O_3 sample, which are characteristic of metallic Pt, indicating Pt particles are relatively large on this sample. For the $Pt/CeO_2/Al_2O_3$ sample, only a weak reflection of Pt is evident, at around 40°. Interestingly, no Pt-related reflection is observed with the Pt/CeO_2 sample, suggesting that Pt is present in a highly dispersed state.

In order to further explore the Pt dispersion state, DRIFTS was used to characterize CO adsorption on the samples after reduction and the results are shown in Fig. 10. From the intensity of the band at 2,075 cm^{-1}, it is clear that the dispersion state of Pt decreases in the order of $Pt/CeO_2 > Pt/CeO_2/Al_2O_3 \gg Pt/Al_2O_3$. These results confirm the stabilization effect of ceria on Pt. Here, it is worth noting that almost no CO adsorption on Pt was observed on Pt/Al_2O_3, indicating very low Pt dispersion, consistent with the XRD results. CO adsorption on a fresh Pt/Al_2O_3 sample (calcined at 500 °C) was also tested, and a very obvious CO adsorption band was observed (not shown here). Therefore, the aging

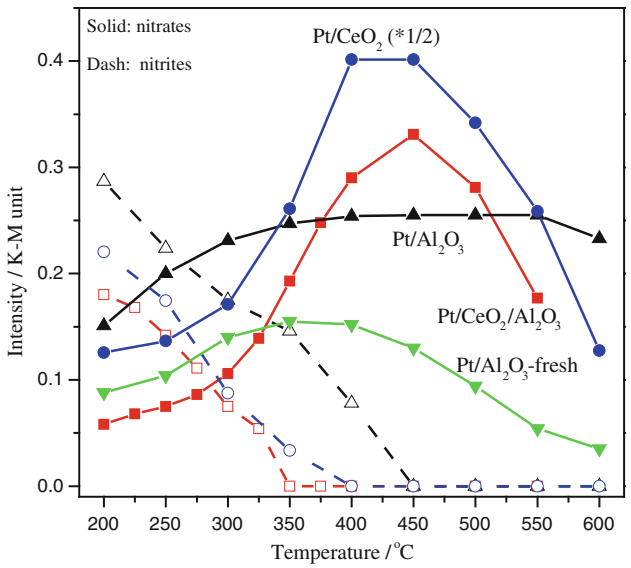

Fig. 8 Intensity of nitrites (*dashed*) and nitrates (*solid*) as a function of temperature for Pt/Al_2O_3 (*black*), Pt/CeO_2 (*blue*), $Pt/CeO_2/Al_2O_3$ (*red*) and fresh Pt/Al_2O_3 (*green*)

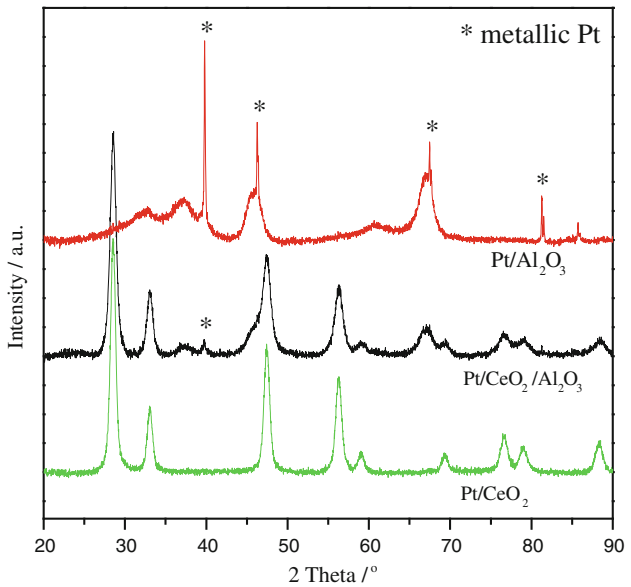

Fig. 9 XRD spectra of Pt/Al_2O_3 (*red*), $Pt/CeO_2/Al_2O_3$ (*black*) and Pt/CeO_2 (*green*)

treatment induces Pt agglomeration. However, ceria significantly reduces Pt sintering over Al_2O_3. In addition, some carbonates were identified, on both the ceria and alumina surfaces [35, 36], and from the types of carbonates, it is deduced that alumina, not ceria, is the most exposed surface on $Pt/CeO_2/Al_2O_3$. This is consistent with the DRIFTS data obtained during NO_x adsorption, since most of the nitrates were adsorbed on the Al_2O_3 surface.

TEM data were also obtained, and the results are shown in Fig. 11. For Pt/Al_2O_3, very large Pt particles, in the

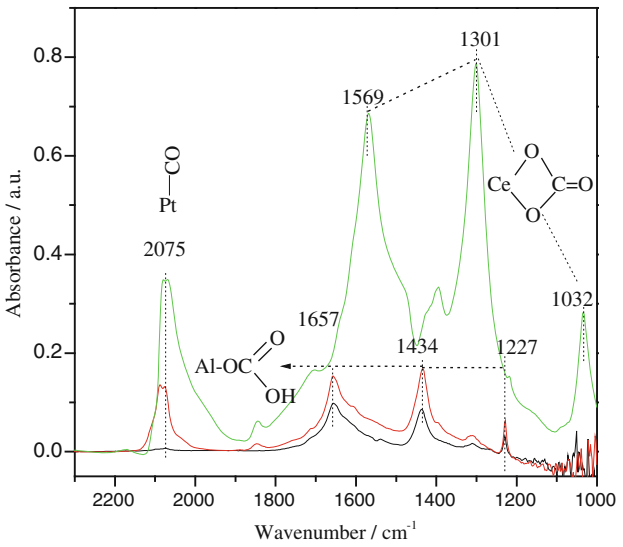

Fig. 10 DRIFTS of CO adsorption over reduced Pt/CeO_2 (*green*), $Pt/CeO_2/Al_2O_3$ (*red*), and Pt/Al_2O_3 (*black*)

range of micrometers, were observed, as shown in Fig. 11a. Such large particles are not present on the $Pt/CeO_2/Al_2O_3$ sample. Interestingly, on $Pt/CeO_2/Al_2O_3$, Pt is present in two separate forms based on the element mapping results in Fig. 11b. Over the Al_2O_3 surface, as shown in area (a), Pt is present as small nanoparticles; while in the area where both ceria and Al_2O_3 are present, area (b), it seems that Pt is preferentially associated with ceria, in a highly dispersed form. Over the Pt/CeO_2 sample, as shown in Fig. 11c, no Pt particles are observed, thus Pt is highly dispersed. According to the literature [26], Pt atoms can be stabilized by the ceria support via the formation of a Pt–O–Ce bond. XPS characterization results from the Pt/CeO_2 sample indicate that Pt is present in an oxidized Pt^{2+} state, with the calibrated binding energy for Pt $4f_{7/2}$ and $4f_{5/2}$ of 72.8 and 76.1 eV, respectively [27], consistent with the Pt–O–Ce interaction. The TEM results are consistent with both XRD and DRIFTS results in terms of Pt state and dispersion.

3.5 Relationship Between Structure and Catalytic Performance

The results of structural characterization indicate that the dispersion decreases in the order of $Pt/CeO_2 > Pt/CeO_2/Al_2O_3 \gg Pt/Al_2O_3$. Interestingly, $Pt/CeO_2/Al_2O_3$, with the medium Pt dispersion, was the most active for NO oxidation. In general, NO oxidation kinetic studies reveal an apparent first order dependence for both NO and O_2, and negative first order for NO_2 [37, 38]. It has also been shown in the literature that turnover frequencies (TOF) are much higher on larger Pt particles than smaller ones, since larger Pt particles bind oxygen adatoms more weakly than small ones, which are more coordinatively unsaturated, allowing

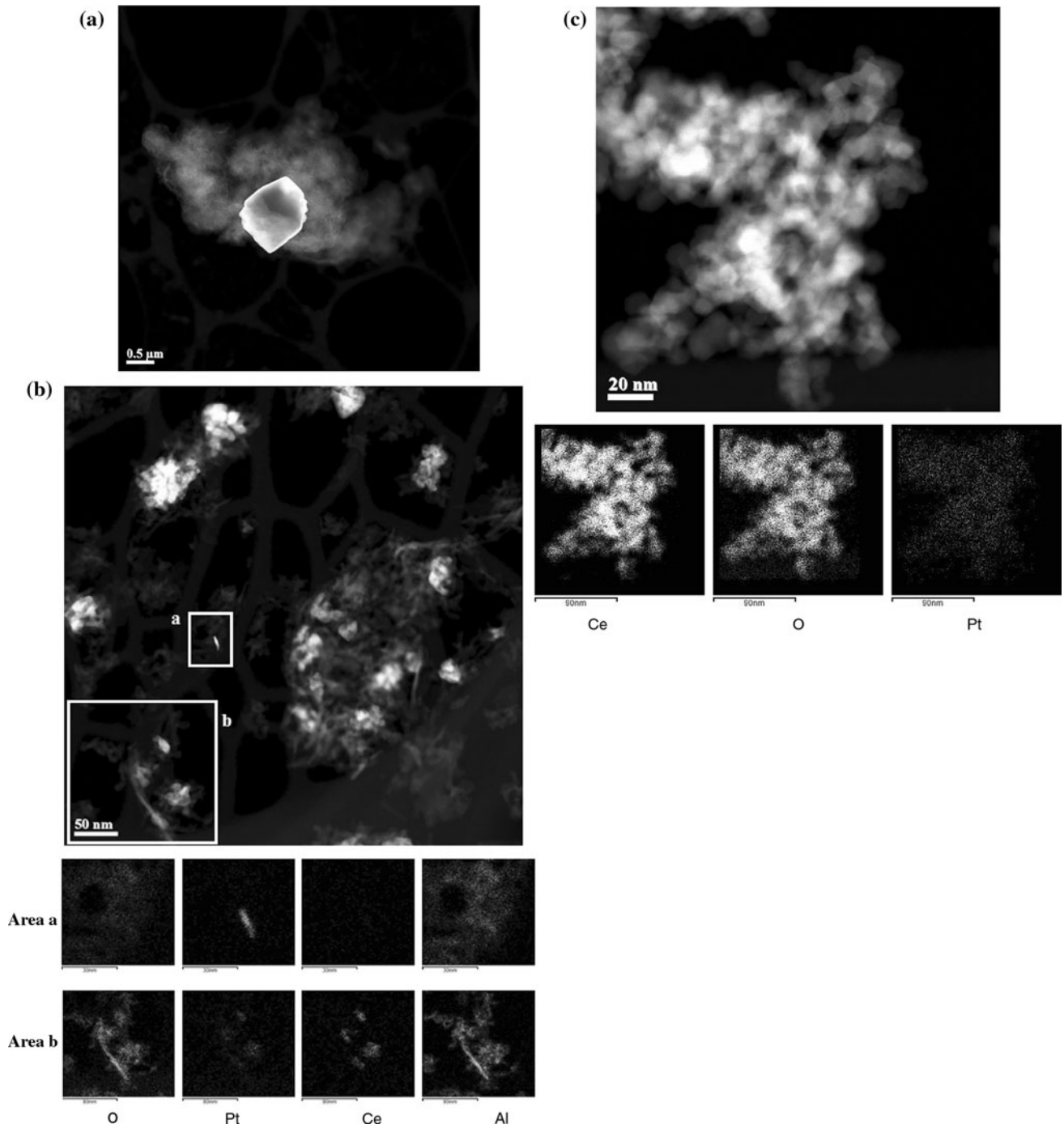

Fig. 11 TEM images and elementary mapping for **a** Pt/Al_2O_3, **b** $Pt/CeO_2/Al_2O_3$ and **c** Pt/CeO_2

easier vacancy site formation and quicker oxygen dissociative activation [38]. Small Pt particles bond oxygen more strongly and furthermore get oxidized by the oxidation product NO_2, leading to a continuous decrease in NO oxidation activity [39]. In other words, since large Pt particles are more oxidation resistant, they are more active toward NO oxidation. Here, the Pt particles on Pt/Al_2O_3 are very large and result in a very high NO oxidation TOF ($\sim$1,763 h^{-1} based on conversion at 200 °C and dispersion measured by H_2 chemisorption), but the low dispersion (less than 1 %) limits the overall conversion. For the Pt/CeO_2 sample, Pt is present in an oxidized form as indicated by XPS, or in other words, oxygen is strongly bound to Pt, which is induced by the strong interaction with the support CeO_2. The NO oxidation TOF over the Pt/CeO_2 sample is quite small (1.8 h^{-1}) and limits overall NO

oxidation. For the $Pt/CeO_2/Al_2O_3$ sample, the presence of CeO_2 limits Pt agglomeration, even for metallic Pt on Al_2O_3, as shown in the TEM results. In general, Pt sintering occurs via Ostwald ripening, and the presence of ceria in the catalysts studied here possibly inhibits migration of Pt atoms through the support due to the strong interaction, thus delaying Pt sintering on Al_2O_3. The nanoscale metallic Pt particles over the Al_2O_3 support, although leading to lower TOF, do give overall higher NO oxidation conversions. As indicated above, NO oxidation to NO_2 is crucial for enhanced NO_x adsorption at low temperature and therefore, $Pt/CeO_2/Al_2O_3$ ends up having the largest low temperature NO_x adsorption capacity.

Besides promoted NO oxidation by influencing the Pt state and dispersion, the other advantage of ceria addition is the introduction of new NO_x adsorption sites. NO_x adsorption on CeO_2 as nitrates was confirmed by DRIFTS; and ceria is more effective for NO_x adsorption than Al_2O_3 on a per surface area basis, which contributes to the observed enhanced NO_x adsorption. This is supported by the comparison of $PtPd/Al_2O_3$ and $Pt/CeO_2/Al_2O_3$ samples. Although both samples show the same NO oxidation activity at 200 °C, $Pt/CeO_2/Al_2O_3$ has a higher NO_x adsorption capacity than $PtPd/Al_2O_3$.

Finally, Pt dispersion also affects surface NO_x species decomposition. As indicated by the NO_x-TPD results, nitrates stored on Pt/CeO_2 decompose at lower temperature than those over CeO_2, indicating the presence of Pt can catalyze surface NO_x species decomposition and NO_x desorption, which is consistent with literature results [40, 41]. Therefore, Pt dispersion will influence NO_x desorption. Due to the high dispersion on the fresh Pt/Al_2O_3 sample relative to the aged Pt/Al_2O_3, the NO_x desorption temperature is more than 100 °C lower on the fresh sample than on the aged sample, as shown by the DRIFTS–TPD results in Fig. 8. On this basis, although NO_x is mainly adsorbed on the Al_2O_3 surface on both aged Pt/Al_2O_3 and aged $Pt/CeO_2/Al_2O_3$ samples, significant differences in NO_x desorption temperatures result from different Pt dispersions. Ceria maintains Pt dispersion over Al_2O_3, thus decreasing the NO_x desorption temperature. Similarly, Pd stabilizes Pt and enhances its dispersion, contributing to the lower NO_x desorption temperature on $PtPd/Al_2O_3$ than Pt/Al_2O_3.

4 Conclusions

Two types of NO_x storage routes exist, via either NO_2 or nitrites as intermediates. For non-Pt/CeO_2 containing samples, there is a good relationship between NO oxidation and NO_x storage capacity, suggesting NO_x storage via the NO_2. While for Pt/CeO_2 containing samples, NO_x can also be stored via a nitrites route, resulting in significant trapping even with low NO oxidation ability. The $Pt/CeO_2/Al_2O_3$ sample shows higher NO oxidation activity and NO_x storage capacity after hydrothermal aging, as compared with Pt/CeO_2 and Pt/Al_2O_3 samples. The combination of CeO_2 and Al_2O_3 results in relatively stabilized Pt, while maintaining its metallic state, thereby improving NO oxidation and subsequent NO_x adsorption. Meanwhile, as compared with Pt/Al_2O_3, the addition of CeO_2 to the formulation introduces new NO_x adsorption sites which are more efficient than those of Al_2O_3. In addition, Pt dispersion influences the stability of the stored nitrates, and highly dispersed Pt promotes or catalyzes surface NO_x species decomposition.

Acknowledgments The authors acknowledge General Motors and the Natural Science and Engineering Research Council of Canada for funding. The authors also thank Michael P. Balogh for XRD and TEM measurements.

References

1. Epling WS, Campell LE, Yezerets A, Currier NW, Parks JE (2004) Catal Rev 46:163
2. Lietti L, Forzatti P, Nova I, Tronconi E (2001) J Catal 204:175
3. Takahashi N, Shinjoh H, Lijina T, Suzuki T (1996) Catal Today 27:63
4. Mahzoul H, Brilhac JF, Gilot P (1999) Appl Catal B 20:47
5. Klingstedt F, Arve K, Eranen K, Murzin DY (2006) Acc Chem Res 39:273
6. Andersen PJ, Chen HY, Fedeyko JM, Weigert E (2010) US Patent US 2010/0267548 A1
7. Xu L, Graham G, McCabe R (2007) Catal Lett 115:108
8. Kikuyama S, Matsukuma I, Kikuchi R, Sasaki K, Eguchi K (2002) Appl Catal 226:23
9. Eguchi K, Kondo T, Hayashi T, Arai H (1998) Appl Catal B 16:69
10. Fornasari G, Trifiro F, Vaccari A, Prinetto F, Ghiotti G, Centi G (2002) Catal Today 75:421
11. Fornasari G, Glockler R, Livi M, Vaccari A (2005) Appl Clay Sci 29:258
12. Centi G, Fornasari G, Gobbi C, Livi M, Trifiro F, Vaccari A (2002) Catal Today 73:287
13. Yu JJ, Jiang Z, Zhu L, Hao ZP, Xu ZP (2006) J Phys Chem B 110:4291
14. Li Q, Meng M, Xian H, Tsubaki N, Li X, Xie Y, Hu T, Zhang J (2010) Environ Sci Technol 44:4747
15. Silletti BA, Adams RT, Sigmon SM, Nikolopoulos A, Spivey JJ, Lamb HH (2006) Catal Today 114:64
16. Li LD, Yu JJ, Hao ZP, Xu ZP (2007) J Phys Chem C 111:10552
17. Eguchi K, Watabe M, Ogata S, Arai H (1996) J Catal 158:420
18. Machida M, Kurogi D, Kijima T (2003) Catal Today 84:201
19. Le Phuc N, Corbos EC, Courtois X, Can F, Marecot P, Duprez D (2009) Appl Catal B 93:12
20. Rohart E, Baca VB, Harle C, Potois C (2008) SAE 2008-01-0450
21. Azambre B, Zenboury L, Koch A, Weber JV (2009) J Phys Chem C 113:13287
22. Azambre B, Atribak I, Lopez AB, Garcia AG (2010) J Phys Chem C 114:13300
23. Choi JS, Partridge WP, Lance MJ, Walker LR, Phil JA, Toops TJ, Finney CEA, Daw CS (2010) Catal Today 151:354

24. Kim CH, Schmid M, Schmieg SJ, Tan J, Li W (2011) SAE 2011-01-1134
25. Nova I, Castoldi L, Lietti L, Tronconi E, Forzatti P, Prinetto F, Ghiotti G (2004) J Catal 222:377
26. Hatanaka M, Takahashi N, Tanabe T, Nagai Y, Dohmae K, Aoki Y, Yoshida T, Shinjoh H (2010) Appl Catal B 99:336
27. Hatanaka M, Takahashi N, Takahashi N, Tanabe T, Nagai Y, Suda A, Shinjoh H (2009) J Catal 226:182
28. Ji Y, Fisk C, Easterling V, Graham U, Poole A, Crocker M, Choi JS, Partridge W, Wilson K (2010) Catal Today 151:362
29. Toops TJ, Smith DB, Epling WS, Parks JE, Partridge WP (2005) Appl Catal B 58:255
30. Nyquist RA, Putzig CL, Leugers MA (1997) The handbook of infrared and Raman spectra of inorganic compounds and organic salts. Academic Press, San Diego
31. Hadjiivanov KI (2000) Catal Rev 42:71
32. Huang SJ, Walters AB, Vannice MA (2000) Appl Catal B 26:101
33. Philipp S, Drochner A, Kunert J, Vogel H, Theis J, Lox ES (2004) Top Catal 30–31:235
34. Ji Y, Toops TJ, Graham UM, Jacobs G, Crocker M (2006) Catal Lett 110:29
35. Holmgren A, Andersson B, Duprez D (1999) Appl Catal B 22:215
36. Toops TJ, Smith DB, Partridge WP (2005) Appl Catal B 58:245
37. Mulla SS, Chen N, Cumaranatunge L, Blau GE, Zemlyanov DY, Deglass WN, Epling WS, Ribeiro FH (2006) J Catal 241:389
38. Weiss BM, Iglesia E (2009) J Phys Chem C 113:13331
39. Bhatia D, McCabe RW, Harold MP, Balakotaiah V (2009) J Catal 266:106
40. James D, Fourre E, Ishii M, Bowker M (2003) Appl Catal B 45:147
41. Prinetto F, Ghiotti G, Nova I, Lietti L, Tronconi E, Forzatti P (2001) J Phys Chem B 105:12732